

## ORIGINAL ARTICLE

# Investigation of the Fluid Induced Forces of Clearance Flow in Canned Motor Reactor Coolant Pump

Yao-Yu Hu<sup>1</sup> • Rui Xu<sup>1</sup> • De-Zhong Wang<sup>1,\*</sup> • Jun-Lian Yin<sup>1</sup> • Yun Long<sup>1</sup>

Received June xx, 201x; revised February xx, 201x; accepted March xx, 201x

© Chinese Mechanical Engineering Society and Springer-Verlag Berlin Heidelberg 2017

**Abstract:** Reactor coolant pump is one of the key components of the coolant loop in a pressurized water reactor system. Its safety relies on the characteristics of the rotordynamic system. For a canned motor reactor coolant pump, the liquid coolant fills up the clearance between the metal cans of the rotor and stator inside the canned motor, forming a clearance flow. The fluid induced forces of the clearance flow in canned motor reactor coolant pump and their effects on the rotordynamic characteristics of the pump are analyzed in this work. A specific purpose 3D code has been developed combining the coordinate transformation and moving reference frame techniques. An experiment rig with similar geometric parameters of canned motor reactor coolant pump is built. The fluid induced forces of the clearance flow are obtained by the newly designed radial force measurement components. The code is validated against experimental results. Results show that clearance flow brings large mass coefficient into the rotordynamic system and the direct stiffness coefficient is negative under the normal operating condition. The rotordynamic stability of canned motor reactor coolant pump does not deteriorate despite the existence of the cross-coupled stiffness coefficient.

**Keywords:** reactor coolant pump • canned motor • rotordynamic coefficient • clearance flow

## 1 Introduction

Canned motor reactor coolant pump (RCP) is one of the

key parts of the reactor coolant system (RCS) in the AP series pressurized water reactor system. In order to achieve safety requirements of the RCS, accurate analysis and evaluation of the rotordynamic characteristics of canned motor RCP in its design phase are mandatory. As illustrated in Fig. 1, canned motor RCP is a vertical rotor system[1]. The entire rotor is immersed in the reactor coolant which is water. It is the fluid in the clearance between the stator and rotor cans that dramatically affects the rotordynamics of canned motor RCP.

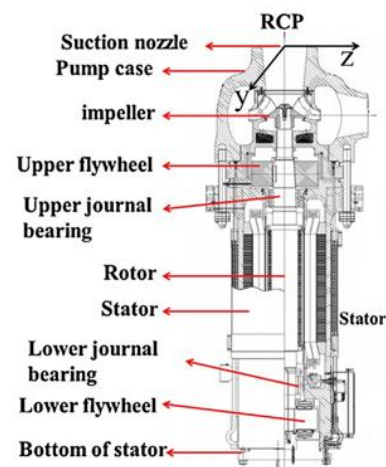


**Fig. 1** canned motor RCP[1].

A typical clearance flow between the stator and rotor cans is shown in Fig. 2. The clearance is filled up with water under 15.5 MPa and approximately 60°C. The water flows upwards by the propulsion of a special auxiliary impeller as shown in Fig. 2. The clearance is a 3D annular shape similar to a plain annular seal. Two key geometric parameters are commonly used to describe such a

Supported by National Natural Science Foundation of China (Grant No. 51576125).

✉ De-Zhong Wang  
dzwang\_sjtu@sina.com

<sup>1</sup> School of Mechanical Engineering, Shanghai Jiao Tong University, No. 800, Dongchuan Rd., Shanghai, 200240, China

clearance flow. They are the clearance-radius ratio ( $CR$ ) and the aspect ratio ( $AR$ ) and are expressed by Eq. (1) and Eq. (2).

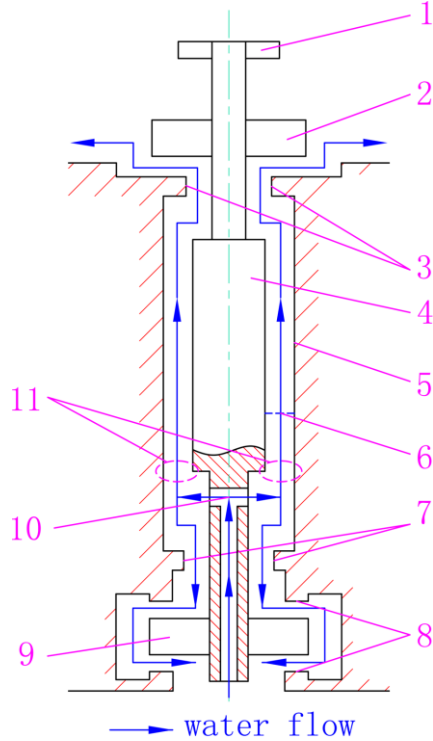


**Fig. 2** Sketch of rotor, stator and clearance flow in canned motor RCP.

1-impeller, 2-upper flywheel, 3-upper journal bearing, 4-rotor, 5-stator, 6-clearance, 7-lower journal bearing, 8-thrust bearing, 9-lower flywheel, 10-auxillary impeller, 11-inlet of clearance flow.

$$CR = \frac{C_0}{r^R} \quad (1)$$

$$AR = \frac{L}{2r^R} \quad (2)$$

where  $C_0$  is the nominal clearance radial width,  $r^R$  is the rotor radius and  $L$  is the clearance length. For canned motor RCP,  $CR$  falls into the range of 0.01 to 0.1 and  $AR$  is about 3.5, respectively. These two values are relatively larger than the common clearances in pumps such as conventional annular seal and hydrodynamic journal bearing.

Lots of work has been done on fluid induced forces of all kinds of annular seals. The fundamental work could be attributed to Fritz, Childs, and Iwatsubo. Fritz[2,3] studied fluid induced forces of a turbulent annular seal through theoretical analysis and experimental test. His model takes account of variable clearance width but ignores the effects

of axial flow. Later, Childs developed a dynamic force model for turbulent plain annular seal based on Hirs' 2D bulk-flow theory[4]. In Childs' model, effects of axial flow, inlet pre-swirl, and inlet pressure loss are all taken into consideration. Childs had conducted lots of work on almost all kinds of turbulent annular seals. Childs' method relies on empirical coefficients which have to be measured for different seal clearances. Given validated empirical coefficients, Childs' model is both accurate and efficient, making it useful throughout several decades, e.g. [5]. Childs' model tells us that axial flow and inlet pre-swirl make significant effects on the fluid induced forces of clearance flow. Iwatsubo[6] began his studies on clearance flow at roughly the same time with Childs' and conducted a series of related work until the 2010s [7]. The theoretical (2D) and experimental work by Kanemori and Iwatsubo[8,9] showed that annular flow with large  $AR$  tends to have negative direct stiffness when the axial flow is relatively weak. For both large  $CR$  and  $AR$  value, Antunes et al[10,11] have systematically studied the fluid induced forces and associated rotordynamic coefficients. Their results also indicate that clearance flow with large  $AR$  would bring significant negative direct stiffness (and added mass) into the rotordynamic system.

Steady state and quasi-steady state computational fluid dynamics (CFD) techniques are utilized to study the fluid induced forces of clearance flow. Dietzen and Nordmann[12] calculated the forces of seals by combining the  $k-\varepsilon$  turbulence model, coordinate transformation, and perturbation analysis. The solution was obtained in 2D. Improved numerical treatments have been used by Rhode, et al[13] and further refined method was developed by Arghir and Frêne[14]. 3D CFD techniques have later been used. Athavale and Przekwas[15] developed the 3D SCISEAL code adopting finite volume method and several turbulence models and was capable of analyzing a variety of clearance flows. Moore analyzed the fluid induced forces of clearance flows based on the multiple/moving frame of reference (MRF) method and special[16] or general[17] purpose 3D CFD packages. The use of general purpose CFD codes with MRF implementation is adopted in a lot of later work due to its accuracy and relatively low cost of computing resource and could be seen in recent work of Subramanian et al[18].

In order to deal with complex rotor motion, 3D transient CFD method should be used. Chochua and Soulas[19] and Yan et al[20] performed transient analysis of a clearance flow with mesh deformation. Yan et al[21] later proposed a novel method that based on Laplace transform. Fluid induced forces of all excitation frequencies could be solved

by only one or two transient CFD runs. The method Wu et al[22] could also produce the desired forces with only two transient simulations with variable-speed whirl motion.

It is notable that some work was done especially for clearance flow with large  $AR$ , e.g. Untaroiu et al[23,24]. Some recent research on clearance flow with large  $AR$  value, e.g. [25] and [26], tend to predict the presence of negative direct stiffness.

Besides clearance length, inlet pre-swirl is another key factor. Fluid induced forces of clearance flow are commonly divided into normal and tangential force components. The effects of inlet pre-swirl on the tangential force components were investigated by Kerr[27], Kirk and Gao[28] and Sun et al[29]. The tangential force prediction of a clearance flow is important to the stability of the underlying rotordynamic system.

Generally, there are two categories of techniques for the measurement of fluid induced forces, based on the methods that enable the whirl motion of the rotor. They are the external excitation and whirl excitation. The tested rotor vibrates under the excitation of external hydraulic or electric shakers for experiments using external excitation. Childs and other researchers[29–31] have utilized this method. The external excitation could also be triggered by the active magnetic bearings, e.g. Kwanka[32] and Sreedharan et al[33]. The whirl excitation method was adopted by Kanemori and Iwatsubo[8,9], Millsaps and Martinez-Sanchez[34] and Zhai et al[35]. External excitation is more flexible and is suitable for high-frequency whirl motion. External excitation system needs relatively complex equipment and sophisticated control logic. By contrast, whirl excitation is easier to implement and the amplitude of the whirl motion could be controlled by modifying the whirl structure. However, the whirl excitation generally works at lower frequency and it usually only produces circular whirl motion.

In the present work, the combination of coordinate transformation and MRF method is utilized to analyze the clearance flow in canned motor RCP with its large  $AR$  and  $CR$  values. A specific purpose code is developed and validated against experiments. The fluid induced forces are measured by adopting the whirl excitation. We designed a new type of bearing structure to measure the radial forces. For the clearance flow in the canned motor RCP, the rotordynamic coefficients and the influence of inlet pre-swirl are calculated by the newly developed code.

## 2 Numerical method

### 2.1 Geometry and coordinate transformation

The target clearance of the present work has a plain annular shape. Figure 3 shows the cross-section of the clearance flow in canned motor RCP. The geometric parameters associated with Fig. 3 and pump operation parameters are listed in Table 1. The parameters of RCP are the same with those used by Hu et al[36]. As shown in Fig. 3, the center of the rotor,  $O$ , is located at the concentric position with respect to the stator. In general operation, the center of rotor drifts to an eccentric position,  $O'$ , with an eccentric distance of  $r_0$  due to excitation such as unbalanced force. Then the motion of the rotor is the combination of rotating along the rotor axis and whirl motion with respect to the stator center. The angular speed of rotating is denoted by  $\omega^R$ , and the whirl angular speed is  $\Omega$ . In Fig. 3, the axis of the rotor is parallel to the  $x$ -axis of the underlying default Cartesian coordinate system. Here, a cylindrical coordinate system,  $(x, r, \theta)$ , with the same  $x$ -axis is set up. The whirl motion of the rotor renders the clearance axial asymmetric. A simple coordinate transformation in  $(x, r, \theta)$  expressed by Eq. (3) is applied to transform the geometry of the clearance back into axial symmetric annular shape as described by the dashed curve in Fig. 3.

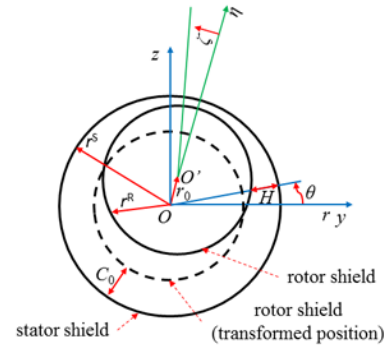


**Fig. 3** Cross section of clearance and coordinate transformation.

**Table 1** Geometric and operation parameters.

Item	Value	
	RCP <sup>a</sup>	Exp <sup>b</sup>
Rotor radius, $r^R$ (m)	0.29	0.05
Stator radius, $r^S$ (m)	0.295	0.051
Nominal clearance, $C_0$ (m)	0.005	0.001
Length, $L$ (m)	2	0.4
Rotating angular speed, $\omega^R$ (rad/s)	188.5	213.63
Inlet mass flow rate (kg/s)	43.9	0.0728
Fluid density, $\rho$ (kg/m <sup>3</sup> )	994.7	997.15
Fluid dynamic viscosity, $\mu$ (Pa·s)	0.00054	8.87e-4
Linear parameter, $\varepsilon_e$	0.1	0.15

<sup>a, b</sup>RCP is for canned motor RCP, Exp is for experiment

$$\begin{aligned}\xi &= x \\ \eta &= r^S - \frac{r^S - r}{H} C_0 \\ \zeta &= \theta\end{aligned}\quad (3)$$

where the target transformed coordinate system is denoted as  $(\xi, \eta, \zeta)$ . In Eq. (3),  $H$  is the clearance width along circumferential coordinate  $\theta$  and is expressed by Eq. (4).  $h_1$  in Eq. (4) serves as a perturbed clearance width variable with a dimensionless linear parameter  $\varepsilon_e$ . Here  $\varepsilon_e h_1$  could be written as Eq. (5). The above coordinate transformation method was proposed by Dietzen and Nordmann[12]. The value of  $\varepsilon_e$  is usually defined as Eq. (6).

$$H = C_0 + \varepsilon_e h_1 \quad (4)$$

$$\varepsilon_e h_1 = -r_0 \cos(\theta) \quad (5)$$

$$\varepsilon_e = \frac{r_0}{C_0} \quad (6)$$

## 2.2 Quasi-steady state model

After coordinate transformation, the geometry becomes axial symmetric. However, the physical process of the whirl motion is unsteady. In this work, the MRF method is also utilized to transform the unsteady nature of the original process into a quasi-steady state problem. Assuming that the entire clearance flow region is rotating along the x-axis with angular speed  $\Omega$ . It means that the flow field rotates in the same manner of the rotor whirl motion. This results in adding new terms in the governing momentum equations in the original cylindrical coordinate system  $(x, r, \theta)$ . For Reynolds averaged Navier-Stokes equations, those new terms are listed in Eq. (7) to Eq. (9) and are enclosed by curly braces.

$$\rho \left[ \frac{\partial u}{\partial t} + \nabla \cdot (\mathbf{u}u) \right] = \nabla \cdot (\mu_{\text{eff}} \nabla u) + s_u^m \quad (7)$$

$$\rho \left[ \frac{\partial v}{\partial t} + \nabla \cdot (\mathbf{u}v) \right] = \nabla \cdot (\mu_{\text{eff}} \nabla v) + s_v^m + \{ \rho \Omega^2 r + 2\rho \Omega w \} \quad (8)$$

$$\rho \left[ \frac{\partial w}{\partial t} + \nabla \cdot (\mathbf{u}w) \right] = \nabla \cdot (\mu_{\text{eff}} \nabla w) + s_w^m + \{ -2\rho \Omega v \} \quad (9)$$

In Eq. (7) to Eq. (9),  $u$ ,  $v$  and  $w$  are the three components of the velocity vector  $\mathbf{u}$  in the coordinate system  $(x, r, \theta)$ .  $t$  represents time.  $\rho$  is the density of the fluid inside the clearance.  $\mu_{\text{eff}}$  is effective viscosity being the sum of dynamic viscosity,  $\mu$ , and turbulent eddy viscosity,  $\mu_t$ .  $s_u^m$ ,  $s_v^m$  and  $s_w^m$  are source terms for each momentum equation. The above quasi-steady state model

was successfully used by Dietzen and Nordmann[37] and Brucato et al[38]. In this work, the coordinate transformation and quasi-steady state model are combined to simplify the original clearance flow.

## 2.3 Computation code and boundary conditions

A specific purpose code with the name of PCF (Perturbed Clearance Flow) is developed to solve the governing equations. Finite volume method with collocated grid is implemented in PCF under the guidance of the work of Versteeg and Malalasekera[39] and Moukalled et al[40]. In PCF, convection and diffusion terms are treated by TVD[41] and central difference schemes, respectively. Turbulence is handled by the SST  $k$ - $\omega$  model with automatic wall treatment, following the work of Menter et al[42].

An issue becomes apparent after we apply the coordinate transformation described by Eq. (3). Since the cylindrical coordinate system is curvilinear, and the target coordinate system of the transformation is a non-orthogonal curvilinear system, the coordinate transformation is, in fact, a special case that involves two curvilinear coordinate systems. This is quite different with the transformation from Cartesian coordinates to curvilinear counterparts that usually found in the literature. Thus, special care should be paid when deriving detailed finite volume method with such coordinate transformation. Considering the additional complexity brought by the coordinate transformation, PCF uses the relatively straightforward the SIMPLE algorithm to cope with pressure-velocity coupling. Moreover, the coordinate transformation affects some key processes associated with SIMPLE algorithm on collocated grid, like the momentum interpolation and the gradient reconstruction. In the context of finite volume method, the implementation of the above mentioned key processes is done by referring to the work of Hong[43] and Qu et al[44].

The PCF code is programmed by C++ and Python languages, with the help of the open-source scientific computing package PETSc[45]. PCF is able to perform automated grid generation and parallel computing.

Boundary conditions are set as follows: The fluid domain has mass flow inlet and static pressure outlet. The outlet pressure is 0 Pa. Both the rotor and stator surfaces are set to be the non-slip smooth wall. The circumferential velocities of the walls are set with respect to the rotating speed of the flow region,  $\Omega$ , the rotating speed of the rotor,  $\omega^R$ , and the geometric parameters. The  $w$  components of the wall velocities are listed in Eq. (10) and Eq. (11), and are illustrated in Fig. 4 and Fig. 5.

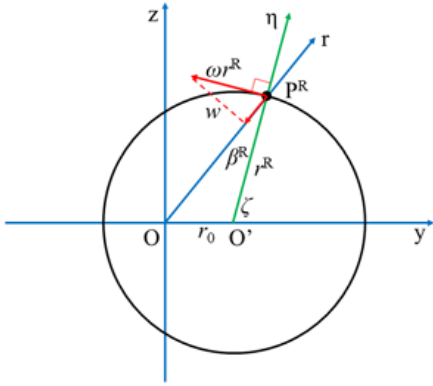


**Fig. 4**  $w$  component of velocity vector on rotor surface.  $P^R$  is a point on rotor surface.

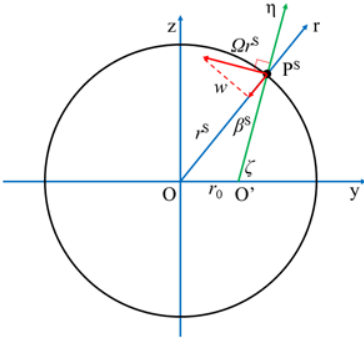


**Fig. 5**  $w$  component of velocity vector on rotor surface.  $P^S$  is a point on stator surface.

$$w = (\omega - \Omega) r^R \sqrt{1 - \sin^2 \beta^R} \quad (10)$$

$$w = -\Omega r^S \sqrt{1 - \sin^2 \beta^S} \quad (11)$$

where  $\beta^R$  and  $\beta^S$  are small angles satisfying Eq. (12) and Eq. (13).

$$\sin \beta^R = \frac{(r_0 \sin \zeta)^2}{\sqrt{(r^R + r_0 \cos \zeta)^2 + (r_0 \sin \zeta)^2}} \quad (12)$$

$$\sin \beta^S = \frac{r_0}{r^S} \sin(|\pi - \zeta|) \quad (13)$$

The  $w$  components given in Eq. (10) and Eq. (11) are similar to those used by Dietzen and Nordmann[37] based on the fact that  $\beta^R$  and  $\beta^S$  are small and their values of sine functions are approximately equal to 1.

Since the geometry of the fluid region is axial symmetric after coordinate transformation, grid generation is extremely convenient and could be easily automated. PCF adopts hexahedron collocated grid. Because there is no longer any curve in the transformed curvilinear coordinate system, very few grids are needed in  $\zeta$  direction. The cell density of 30x20x160 (for  $\zeta$ ,  $\eta$  and  $\zeta$  directions) is used to

perform simulations against test results. The geometric and operation parameters are also listed in Table 1. PCF uses the normalized root-mean square (RMS) residual to detect convergence. The convergence limit is  $10^{-5}$ .

### 3 Experiment

An experiment rig with comparable  $CR$  and  $AR$  values to canned motor RCP is set up. As illustrated in Fig. 6, the experiment rig is designed to have a vertical shaft similar to the canned motor RCP. At the test section, the rotor is installed inside the stator, forming a clearance flow. Water at room temperature is the tested fluid. The fluid flows upwards in the test section.

The rotor could perform combined rotating and whirling motions which means that the rotor rotates about its own axis and whirls with respect to the axis of the stator simultaneously. This combined motion is achieved by the “shaft-in-shaft” configuration of the upper and lower whirl bearing components (WBC). This “shaft-in-shaft” concept is already used in many other works, e.g. Kanemori and Iwatsubo[8], Zhai et al[35]. The detailed description of the key components of the test rig, the measured parameters and the methods to perform the measurements are presented in Appendix A.

The fluid induced forces of the clearance flow are determined in a two-steps process. First, the rig is operated without fluid inside the clearance. And the radial forces, rotating speed of the test rotor and its whirling speeds are recorded. For the next step, the tests are performed with the same rotating and whirling speeds as the first step, and with fluid filled up the clearance. The fluid induced forces are then obtained by calculating the differences between the measured forces in those two steps.

### 4 Comparison between the simulation and experiment

The fluid induced forces are measured on the experiment rig with single rotating speed and a range of whirling speeds. The numerical simulations are performed with the same operation settings and the same geometrical parameters with the experiments. The fluid induced forces depend on the frequency of the whirl motion. Let  $WR = \Omega/\omega^R$ . PCF uses the same  $WR$  values with the experiments.

Due to the eccentric whirl motion of the rotor, the pressure profile on the rotor surface is axial asymmetric. The fluid induced forces are obtained by integrating the pressure on the rotor surface. Typically, fluid induced



forces are represented by two force components in perpendicular directions. They are the radial force,  $F_n$ , and the tangential force,  $F_t$ , respectively. It is convenient to express the  $F_n$  and  $F_t$  in terms of  $G_s$ , which are expressed by Eq. (14). At a given time,  $F_n$  is along the line which is determined by joining the points O and O' in Fig. 3.  $F_t$  is orthogonal to  $F_n$  and is in the anticlockwise direction.  $F_n$  and  $F_t$  are commonly modeled as two quadratic polynomials in terms of  $\Omega$  and are expressed in Eq. (15) [23,24].

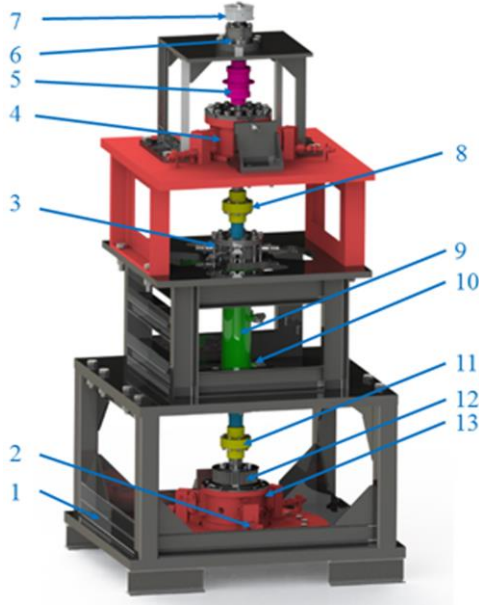


**Fig. 6** Overview of the experiment rig.

1-supporting frame, 2-dynamic force sensor, 3-outlet component, 4-upper whirl bearing component, 5-flexible coupling, 6-top bearing component, 7- synchronous pulley, 8-rigid coupling, 9-test section, 10-pressure and displacement sensors, 11-rigid coupling, 12-whirl pulley, 13-lower whirl bearing components.

$$G_n = \frac{F_n}{r_0}, G_t = \frac{F_t}{r_0}, G_f = \sqrt{G_n^2 + G_t^2} \quad (14)$$

$$\begin{Bmatrix} G_n \\ G_t \end{Bmatrix} = \frac{1}{r_0} \begin{Bmatrix} F_n \\ F_t \end{Bmatrix} = \begin{Bmatrix} M^d \Omega^2 - c^d \Omega - K^d \\ m^d \Omega^2 - C^d \Omega + k^d \end{Bmatrix} \quad (15)$$

where  $M^d$ ,  $C^d$ , and  $K^d$  are the direct mass, damping and stiffness coefficients, respectively.  $m^d$ ,  $c^d$ , and  $k^d$  in Eq. (15) are the cross-coupled mass, damping and stiffness coefficients. The  $G_f$  values obtained by the experiments and PCF are illustrated in Fig. 7. Good agreement is found between the  $F_n$  curves of the experiment and the simulation. However, relatively larger discrepancies are present between the  $F_t$  curves. The main reason for this deviation is that the measurement of  $F_t$  is affected by the mechanical

seals which are used when the clearance is filled with fluid. This makes the tested values of  $F_t$  tend to be larger.

Using Eq. (15), one can easily calculate all the rotordynamic coefficients by curve fitting technique. The results of the rotordynamic coefficients obtained by the experiments and numerical simulations are listed in Table 2. From the current experimental and simulation results,  $K^d$  is negative. The  $F_t$  curve in Fig. 7 reduces to a straight line, indicating that  $m^d$  value in Eq. (15) should be close to 0. This is also confirmed in Table 2. In fact,  $m^d$  is assumed to be 0 in lots of previous work, e.g. [4,22,46].

## 5 Fluid induced forces of clearance flow in canned motor RCP

After being validated by the experiment, PCF is further utilized to analyze the clearance flow in the canned motor RCP. Before computing the fluid induced forces of clearance flow in canned motor RCP, the inlet pre-swirl effect should be properly considered since the presence of the auxiliary impeller which directly affects the inlet pre-swirl of the clearance flow. The method proposed by Hu et al[36] is built into PCF to deal with the inlet pre-swirl. Let  $IR$  be the inlet pre-swirl ratio defined as Eq. (16).

$$IR = \frac{w_0}{r^R \omega^R} \quad (16)$$

where  $w_0$  is the circumferential velocity at the center of clearance on the inlet of clearance flow. The  $IR$  value obtained by Hu et al[36] is adopted here since the geometry and operation parameters are identical. Then  $IR$  is 0.36.

Similar to the previous section, the calculated  $F_n$  and  $F_t$  of various  $WR$  values are shown as two curves in Fig. 8.

**Table 2** Rotordynamic coefficients.

Rotordynamic coefficient	$M^d$ (kg)	$m^d$ (kg)	$C^d$ (Ns/m)	$c^d$ (Ns/m)	$K^d$ (N/m)	$k^d$ (N/m)
Experiment	1.16e2	1.07	9.71e3	2.48e4	-1.18e6	9.67e5
PCF	1.10e2	1.39	6.60e3	2.38e4	-1.13e6	7.10e5

Using Eq. (15) and Fig. 8, one can easily calculate the value of  $M^d$  by curve fitting technique. From the current results of clearance flow in canned motor RCP,  $M^d$  is approximately  $2.6 \times 10^4$  kg.  $M^d$  value with the same magnitude could be obtained through theoretical prediction such as that proposed by Antunes et al[10], with the fact that substantial added mass is present in the clearance flow

of canned motor RCP. This phenomenon is also manifested in the experiment. As listed in Table 2, the  $M^d$  value of the experiment is about  $10^2$  kg. It is significantly larger than the weight of the fluid filling the space which is occupied by the rotor.

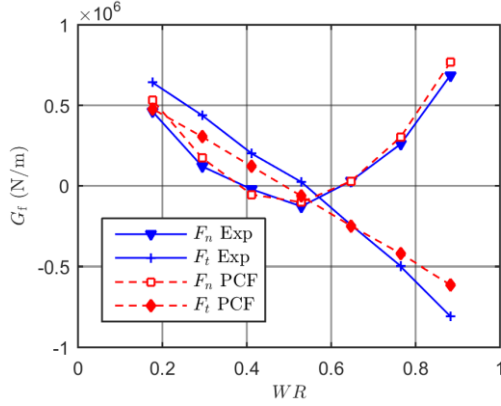


Fig. 7  $G$  values of PCF and experiment.

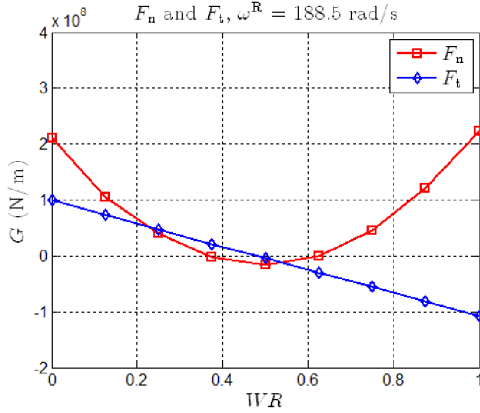


Fig. 8  $F_t$  and  $F_n$  of clearance flow in canned motor RCP,  $\omega^R = 188.5$  rad/s.

From the result in Fig. 8, the associated  $K^d$  value is negative. This is consistent with the conjecture that clearance flow with large  $AR$  value tends to bring negative direct stiffness into the underlying rotordynamic system. This is actually an undesirable feature for the canned motor RCP. Negative direct stiffness causes additional radial load on bearings. Further, the negative  $K^d$  and large  $M^d$  values together lower the overall stiffness or modal frequency of the rotordynamic system of canned motor RCP.

The cross-coupled coefficient  $k^d$  directly links to the stability of the rotordynamic system and is vital to canned motor RCP. Its value reveals itself when  $\Omega = 0$  in Eq. (15). It is believed that the major cause of  $k^d$  is the fluid circulation inside the clearance along the circumferential direction. For clearance flow with relatively small  $AR$

value,  $k^d$  is significantly affected by inlet pre-swirl because the fluid usually has not enough time to reach the fully developed condition after it has been squeezed into the clearance. For canned motor RCP, however, the effect of inlet pre-swirl may not be so notable since the  $AR$  value is so large that fluid could easily achieve the fully developed condition in normal pump operation. Supposing that no inlet pre-swirl is present at the inlet of clearance flow in the canned motor RCP in question, calculate the  $k^d$  value by PCF and compare it to the  $k^d$  value with inlet pre-swirl effect. The  $k^d$  with inlet pre-swirl is  $9.93 \times 10^7$  N/m and the counterpart is  $9.78 \times 10^7$  N/m. Little change is brought by inlet pre-swirl for such long clearance flow in canned motor RCP.

When evaluating the effect of a clearance flow on the stability of a rotordynamic system, the effective damping and whirl frequency ratio could be used as indicators. Eq.(17) and Eq.(18) define these two coefficients. Childs proposed these coefficients and still used them in his recent work, e.g. [26]. For a well-designed clearance flow, it is better to have  $C_{\text{eff}}^d > 0$  and  $f_{\text{wfr}} < 1$ , meaning the clearance flow does not weaken the stability characteristics of the rotordynamic system. Based on the fluid induced force analysis of the clearance flow in canned motor RCP in question, the resulting values of  $C_{\text{eff}}^d$  and  $f_{\text{wfr}}$  are  $5.8 \times 10^5$  and 0.48, respectively. These two values indicate that despite having significant cross-coupled stiffness, the overall effect of the clearance flow on the rotordynamic stability is positive. This positive nature could be attributed to the direct damping coefficient,  $C^d$  since its value is large enough to overcome destabilizing effects from  $k^d$ .

$$C_{\text{eff}}^d = C^d - \frac{k^d}{\omega^R} \quad (17)$$

$$f_{\text{wfr}} = \frac{k^d}{C^d \omega^R} \quad (18)$$

## 6 Conclusions

A specific purpose code, PCF, which combines the coordinate transformation and moving reference frame techniques is developed in this study. An experiment rig covering the  $CR$  and  $AR$  values of canned motor RCP is built. The fluid induced forces are obtained by the newly developed radial force measurement components. The code is validated against experiments. The flow inside the clearance of canned motor RCP is investigated numerically by PCF. Several conclusions could be summarized as follows.

- The clearance flow in canned motor RCP brings

significant mass coefficient into the dynamic system of the pump.

- For the current design of canned motor RCP, the direct stiffness of the clearance flow is negative.
- Under the normal operating condition of canned motor RCP, the cross-coupled stiffness of the clearance flow is hardly affected by the inlet pre-swirl of the auxiliary impeller.
- The stability of the rotordynamic system of canned motor RCP does not decrease with respect to the clearance flow.

## References

- [1] D Cheng, ZQ Yao, YB Xue, et al. Numerical study on seismic response of the reactor coolant pump in Advanced Passive Pressurized Water Reactor. *Nuclear Engineering and Design*, 2014, 278: 39–49.
- [2] RJ Fritz. The effects of an annular fluid on the vibrations of a long rotor, part 1—theory. *Journal of Basic Engineering*, 1970, 92(4): 923–929.
- [3] RJ Fritz. The Effects of an Annular Fluid on the Vibrations of a Long Rotor, Part 2—Test. *ASME J. Basic Eng*, 1970, 92: 930–937.
- [4] DW Childs. Dynamic analysis of turbulent annular seals based on Hirs' lubrication equation. *Journal of lubrication technology*, 1983, 105(3): 429–436.
- [5] DW Childs, JE Mclean, M Zhang, et al. Rotordynamic performance of a negative-swirl brake for a tooth-on-stator labyrinth seal. *Journal of Engineering for Gas Turbines and Power*, 2016, 138(6): 062505.
- [6] T Iwatsubo. Evaluation of instability forces of labyrinth seals in turbines or compressors. *NASA. Lewis Res.* 1980, No. 19800021214.
- [7] T Iwatsubo and H Ishimaru. Consideration of Whirl Frequency Ratio and Effective Damping Coefficient of Seal. *Journal of System Design and Dynamics*, 2010, 4(1): 177–188.
- [8] Y KANEMORI and T IWATSUBO. Experimental Study of Dynamical Characteristics of a Long Annular Seal (In the Case of Concentric Rotor and Outer Cylinder). *JSME international journal. Ser. 2, Fluids engineering, heat transfer, power, combustion, thermophysical properties*, 1989, 32(2): 218–224.
- [9] Y Kanemori and T Iwatsubo. Rotordynamic analysis of submerged motor pumps: Influence of long seal on the stability of fluid machinery. *JSME international journal. Ser. C, Dynamics, control, robotics, design and manufacturing*, 1994, 37(1): 193–201.
- [10] J Antunes, F Axisa and T Grunenwald. Dynamics of rotors immersed in eccentric annular flow. Part 1: Theory. *Journal of Fluids and Structures*, 1996, 10(8): 893–918.
- [11] T Grunenwald, F Axisa, G Bennett, et al. Dynamics of rotors immersed in eccentric annular flow. Part 2: Experiments. *Journal of fluids and structures*, 1996, 10(8): 919–944.
- [12] FJ Dietzen and R Nordmann. Calculating rotordynamic coefficients of seals by finite-difference techniques. *Journal of Tribology*, 1987, 109(3): 388–394.
- [13] DL Rhode, SJ Hensel and MJ Guidry. Labyrinth seal rotordynamic forces using a three-dimensional Navier-Stokes code. *Journal of tribology*, 1992, 114(4): 683–689.
- [14] M Arghir and J Frêne. A quasi-two-dimensional method for the rotordynamic analysis of centered labyrinth liquid seals. *Journal of engineering for gas turbines and power*, 1999, 121(1): 144–152.
- [15] M Athavale and A Przekwas. SCISEAL: A CFD code for analysis of fluid dynamic forces in seals. 1994, :
- [16] JJ Moore and AB Palazzolo. Rotordynamic force prediction of whirling centrifugal impeller shroud passages using computational fluid dynamic techniques. 1999. p V004T03A036–V004T03A036.
- [17] JJ Moore, DL Ransom and F Viana. Rotordynamic Force Prediction of Centrifugal Compressor Impellers Using Computational Fluid Dynamics. *Journal of Engineering for Gas Turbines and Power*, 2010, 133(4): 042504–042504.
- [18] S Subramanian, AS Sekhar and BVSSS Prasad. Rotordynamic characteristics of rotating labyrinth gas turbine seal with centrifugal growth. *Tribology International*, 2016, 97: 349–59.
- [19] G Chochua and TA Soulas. Numerical Modeling of Rotordynamic Coefficients for Deliberately Roughened Stator Gas Annular Seals. *Journal of Tribology*, 2006, 129(2): 424–9.
- [20] X Yan, J Li and Z Feng. Investigations on the Rotordynamic Characteristics of a Hole-Pattern Seal Using Transient CFD and Periodic Circular Orbit Model. *Journal of Vibration and Acoustics*, 2011, 133(4): 041007.
- [21] X Yan, K He, J Li, et al. A Generalized Prediction Method for Rotordynamic Coefficients of Annular Gas Seals. *Journal of Engineering for Gas Turbines and Power*, 2015, 137(9): 092506.
- [22] D Wu, X Jiang, S Li, et al. A new transient CFD method for determining the dynamic coefficients of liquid annular seals. *Journal of Mechanical Science and Technology*, 2016, 30(8): 3477–86.
- [23] A Untaroiu, CD Untaroiu, HG Wood, et al. Numerical modeling of fluid-induced rotordynamic forces in seals with large aspect ratios. *Journal of Engineering for Gas Turbines and Power*, 2013, 135(1): 012501.
- [24] A Untaroiu, V Hayrapetian, CD Untaroiu, et al. Fluid-induced forces in pump liquid seals with large aspect ratio. *ASME-JSME-KSME 2011 Joint Fluids Engineering Conference*, Hamamatsu, Shizuoka, JAPAN, July 24, 2011. pp 455–463.
- [25] PD Brown and DW Childs. Measurement Versus Predictions of Rotordynamic Coefficients of a Hole-Pattern Gas Seal With Negative Preswirl. *Journal of Engineering for Gas Turbines and Power*, 2012, 134(12): 122503.
- [26] NJ Mehta and DW Childs. Measured Comparison of Leakage and Rotordynamic Characteristics for a Slanted-Tooth and a Straight-Tooth Labyrinth Seal. *Journal of Engineering for Gas Turbines and Power*, 2014, 136(1): 012501.
- [27] BG Kerr. Experimental and theoretical rotordynamic coefficients and leakage of straight smooth annular gas seals. *Texas A&M University*, 2005.
- [28] G Kirk and R Gao. Influence of Preswirl on Rotordynamic Characteristics of Labyrinth Seals. *Tribology Transactions*, 2012, 55(3): 357–64.
- [29] D Sun, S Wang, Z Xiao, et al. Measurement versus predictions of rotordynamic coefficients of seal with swirl brakes. *Mechanism and Machine Theory*, 2015, 94: 188–99.
- [30] BH Ertas, A Delgado and G Vannini. Rotordynamic force coefficients for three types of annular gas seals with inlet preswirl and high differential pressure ratio. *Journal of Engineering for Gas Turbines and Power*, 2012, 134(4): 042503.
- [31] P Jolly, A Hassini, M Arghir, et al. Experimental and Theoretical Rotordynamic Coefficients of Smooth and Round-Hole Pattern



- Water Fed Annular Seals. 2014, : V07BT32A013.
- [32] K Kwanka. Rotordynamic Coefficients of Short Labyrinth Gas Seals—General Dependency on Geometric and Physical Parameters. *Tribology Transactions*, 2007, 50(4): 558–63.
- [33] SS Sreedharan, G Vannini and H Mistry. CFD Assessment of Rotordynamic Coefficients in Labyrinth Seals. 2014, : V07BT32A022.
- [34] KT Millsaps and M Martinez-Sanchez. Rotordynamic forces in labyrinth seals: Theory and experiment. 1994, :
- [35] L Zhai, G Wu, X Wei, et al. Theoretical and experimental analysis for leakage rate and dynamic characteristics of herringbone-grooved liquid seals. *Proceedings of the Institution of Mechanical Engineers, Part J: Journal of Engineering Tribology*, 2015, 229(7): 849–60.
- [36] Y Hu, D Wang, J Yin, et al. Numerical Analysis of Rotordynamic Coefficients of Annular Flow in Canned Motor RCP. 2014, : V001T03A018.
- [37] FJ Dietzen and R Nordmann. A 3-dimensional finite-difference method for calculating the dynamic coefficients of seals. *The Fifth Workshop on Rotordynamic Instability Problems in High-Performance Turbomachinery*, Texas, USA, February 1, 1989. p IV-1.
- [38] A Brucato, M Ciofalo, F Grisafi, et al. Numerical prediction of flow fields in baffled stirred vessels: a comparison of alternative modelling approaches. *Chemical Engineering Science*, 1998, 53(21): 3653–3684.
- [39] HK Versteeg and W Malalasekera. An introduction to computational fluid dynamics: the finite volume method. *Pearson Education*, 2007.
- [40] F Moukalled, L Mangani and M Darwish. The Finite Volume Method in Computational Fluid Dynamics: An Advanced Introduction with OpenFOAM® and Matlab. *Springer*, 2015.
- [41] MS Darwish and F Moukalled. TVD schemes for unstructured grids. *International Journal of Heat and Mass Transfer*, 2003, 46(4): 599–611.
- [42] F Menter, JC Ferreira, T Esch, et al. The SST turbulence model with improved wall treatment for heat transfer predictions in gas turbines. 2003. pp 2–7.
- [43] C-P Hong. Computer modelling of heat and fluid flow in materials processing. *CRC Press*, 2004.
- [44] ZG Qu, WQ Tao and YL He. An Improved Numerical Scheme for the SIMPLER Method on NonOrthogonal Curvilinear Coordinates: SIMPLERM. *Numerical Heat Transfer, Part B: Fundamentals*, 2007, 51(1): 43–66.
- [45] S Balay, S Abhyankar, MF Adams, et al. PETSc Web page. [2016] <http://www.mcs.anl.gov/petsc>.
- [46] T Staubli and M Bissig. Numerically calculated rotor dynamic coefficients of a pump rotor side space. 2001. pp 20–24.

### Biographical notes

**Yao-Yu Hu**, born in 1986, is currently a Ph.D. at *Shanghai Jiao Tong University, China*. His research interests include computational fluid dynamics, internal flow of turbomachinery, rotordynamics and hydrodynamic lubrication.  
E-mail: huyaoyu@sjtu.edu.cn

**Rui Xu**, born in 1990, is currently a Ph.D. candidate at *Shanghai Jiao Tong University, China*.  
E-mail: sharry0727@sjtu.edu.cn

**De-Zhong Wang**, born in 1962, is currently a professor at *Shanghai Jiao Tong University, China*.  
E-mail: dzwang\_sjtu@sina.com

**Jun-Lian Yin**, born in 1984, is currently an associate professor at *Shanghai Jiao Tong University, China*.  
E-mail: jlyin@sjtu.edu.cn

**Yun Long**, born in 1988, is currently a Ph.D. candidate at *Shanghai Jiao Tong University, China*.  
E-mail: longyunjs@sjtu.edu.cn

### Appendix A

Generally, the rotor sits on an intermediate bearing housing (IBH) which sits on the outer supporting components. The trick is that the IBH is deliberately made to be in an eccentric tube shape. There are roller bearings between the rotor and the IBH, and between the IBH and the outer supporting components. Therefore, the rotor can rotate freely in side the IBH and whirl as required once the eccentric IBH rotates at the same time.

To further explain the design and mechanism of the WBC the cross-sectional sketch of the lower WBC is shown in Fig. 9. The IBH consists of three main components: the outer tube, the inner tube, and the whirl pulley. As described previously, the rotor is connected to the IBH by roller bearings (Part 1 and 6 in Fig. 9). And the IBH is further connected to the outer supporting components by another set of roller bearings (Part 10). A belt will be installed on the whirl pulley of the IBH. This belt drives the IBH to rotate.

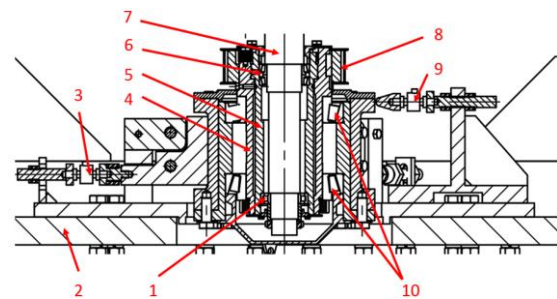


**Fig. 9** The cross-sectional sketch of the lower whirl bearing components (WBC).

1-roller bearing, 2-outer supporting components, 3-dynamic force sensor, 4-outer tube, 5-inner tube, 6-roller bearings, 7-rotor, 8-whirl pulley, 9-dynamic force sensor, 10-roller bearings.

The outer and inner tubes are designed to be eccentric tubes as shown in Fig. 10, and they are manufactured and assembled with great care and precision. These two tubes have the same eccentricity, and they form the maximum total eccentricity,  $e_m$  when they are assembled as of Fig. 10

(c). The eccentricity of the rotor with respect to the stator is adjustable and can be tuned by installing these two tubes with different relative angles. Thus the rotor eccentricity can vary from the concentric condition (Fig. 10 (a)) to maximum eccentricity condition. The structure of the upper WBC is essentially the same. The relative angles between the outer and inner tubes are set and tuned so that the lower and upper WBCs have the same rotor eccentricity. Then the relative angle is locked by pin bolts. In reality, it is extremely difficult to set up the experiment with specific eccentricity and it may cost a whole day to do this fine-tuning task.

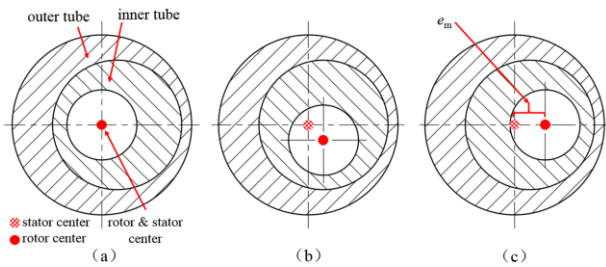


**Fig. 10** Conceptual sketch of the outer and inner tubes.  
(a) concentric position, (b) intermediate position, (c) position of maximum eccentricity.

The power transmission diagram in Fig. 11 shows how the rotating components work. The power for the rotation of the test rotor is provided by the rotation motor and transmitted through a flexible coupling. The flexible coupling has the ability to withstand the eccentric whirl motion of the test rotor, and at the same time, make little effect on the whirl motion. There are two synchronous belts that connect the upper and lower WBCs to a timing shaft. This timing shaft has two synchronous pulleys which are exactly the same with the pulleys on the WBCs. The belts are further preloaded to maintain its tension. All the belts and pulleys are installed so that the phase angles of the WBCs are the same and they rotate simultaneously. A whirl motor is connected with the timing shaft and drives the shaft. The two motors are separately controlled by two frequency inverters and the rotating speeds are measured individually.

On the experiment rig several parameters other than the rotating speeds of the test rotor and the timing rotor, are measured. An electromagnetic flowmeter is used to measure the axial flow rate in the clearance. The axial pressure drop of the fluid across the clearance and the inlet pressure loss caused by the sudden contraction at the inlet of the clearance are measured by pressure difference sensors. There is a thermal resistance thermometer at the inlet of the clearance to test the average inlet temperature

of the fluid. The motion of the rotor is measured by 4 eddy-current probes, which are arranged in 2 groups. One group is installed in the vicinity of the clearance inlet and the other group is near the outlet. The two probes in each group are placed perpendicularly and measure the displacements along two orthogonal axes. In this way, the trajectory of the test rotor could be reconstructed by combining the data of the two displacement probes of the same group. Since the eddy-current probe exhibits different sensitivity while it is testing different type of metals, we conducted calibration using the actual test rotor for each eddy current probe. The final and the most difficult physical parameter to be tested is the radial force the clearance fluid acts on the test rotor. The difficulties come from the fact that the force sensor must be the final supporting component of the bearing if the measurement is done on the stationary component. The task is made even harder for radial force testing in a vertical shaft configuration. Thus, the supporting component should only balance the weight of the rig, leaving the degree of freedom in the radial direction free and disturbing the radial force test as little as possible. In this work, we invent a set of special components to measure the radial force and give it the name of radial force measurement components (RFMC).

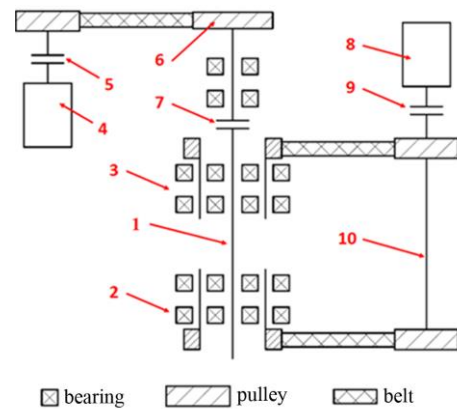


**Fig. 11** Power transmission diagram of the experiment rig.  
1-test rotor, 2-lower whirl bearing components, 3-upper whirl bearing components, 4-rotation motor, 5-coupling, 6-synchronous pulley, 7-flexible coupling, 8-whirl motor, 9-coupling, 10-timing shaft.

The radial force is measured at the stationary parts. As illustrated in Fig. 12, the RFMC consists of structural components and sensors. Every WBC has one RFMC which has three legs, one of these legs is shown in Fig. 12. First of all, there are in fact two cranks (Part 4 in Fig. 12) on one leg, one of the cranks is hidden in order to reveal

the other components in the figure. The leg is suspended by the cranks, pins and roller bearings. There are no direct contacts of friction between the leg and the suspension lever, and the stationary bearing housing (Part 1 in Fig. 12) could move a little bit like a swing if the dynamic force sensor (Part 8 in Fig. 12) is not installed. This configuration allows radial movement and balances the weight of the rotor at the same time. The swinging movement is restrained after all the dynamic force sensors are installed and pre-loaded. When the stationary bearing housing has the trend to move in the direction marked by the blue dashed arrows in Fig. 12, the dynamic force sensors will block the movement and measure the force needed to balance the movement.

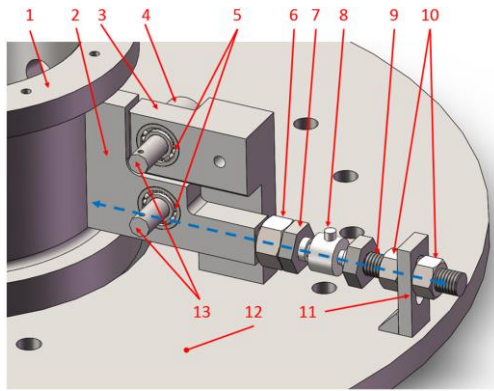


**Fig. 12** One leg of the RFMC.

1-stationary bearing housing, 2-leg, 3-suspension lever, 4-crank, 5-roller bearings, 6-nut, 7-screw bolt, 8-dynamic force sensor, 9-screw bolt, 10-nuts, 11-vertical baffle, 12-base plate, 13-pins.

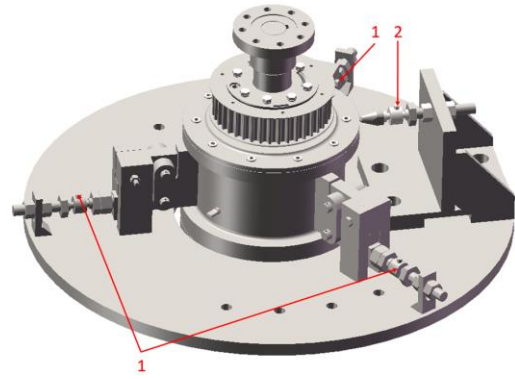


**Fig. 13** Radial force measurement components (RFMC).

1-dynamic force sensors on the legs, 2-auxiliary dynamic force sensor.

Figure 13 shows the overview of the RFMC. The three legs are positioned evenly around the stationary bearing housing. Since the vertical level of the legs is different from the height of the pulley on the WBC, the radial force of the belt will exert a torque with respect to the legs. The whole WBC has a trend of incline in the direction of the belt. There is an auxiliary dynamic force sensor (Part 2 in Fig. 13) in the RFMC. This auxiliary dynamic force sensor is used to resist the torque from the pulley and maintain the upright position of the WBC. The force signals of all the force sensors are recorded by the data acquisition device and are projected to the two axes with the same directions of the eddy-current displacement probes in the post-process stage.